SPIE. OPTICS+ OPTOELECTRONICS

TECHNICAL PROGRAMME

Optics +
Optoelectronics 2019

# TECHNICAL PROGRAMME

**1 - 4 April 2019**

**Exhibition: 2 – 3 April 2019**

Clarion Congress Hotel
Prague, Czech Republic

**spie.org/eoo**

SPIE Optics and Optoelectronics 2019, paper 11028-18

# Do you need a tunable laser for resonant cavity optical sensors?

Mohamed Najih, Rania Gamal, and Andrew Kirk

Electrical and Computer Engineering, McGill University, Montréal, QC, Canada

## ABSTRACT

By measuring the shift in the resonant frequency of whispering gallery modes in an optical microcavity, it is possible to obtain very high sensitivity to changes in the properties of the surrounding medium and the sensor surface. However, a narrow linewidth tunable laser is typically required in order to track the frequency shift. This significantly increases the cost and complexity of such systems. Phase shift cavity ring down spectroscopy (PS-CRDS) represents an alternative approach. In PS-CRDS the interrogating optical signal is sinusoidally modulated and the shift in the phase of the detected signal (rather than the shift in the cavity resonant wavelength) provides information about changes in the cavity properties. PS-CRDS has previously been successfully implemented in resonant optical microcavities, but a tunable laser was still used in order to maintain coupling to the cavity resonance. Here we consider the use of a broadband optical source (e.g. a diode laser or LED) to interrogate the cavity using the PS-CRDS principle. The spectrum of the source always spans more than one cavity resonance and so does not need to be tuned as the cavity resonances shift. We undertake an analytical and experimental investigation to evaluate the effectiveness of this approach and compare it to traditional interrogation methods in terms of sensitivity and signal-to-noise ratio. We focus in particular on the implementation of a resonant cavity biosensor in silicon photonics ring resonators. The results of the study show that the sensitivity to changes in cavity mode loss is slightly lower than when a narrow linewidth source is used, and that sensitivity to changes in the effective refractive index is very significantly reduced. We will discuss the implications of these results in terms of suitable applications of this technique, and the improved potential for integration that the low coherence source brings.

**Keywords:** Silicon photonics, biosensing, PS-CRDS, Whispering Gallery Modes

## 1. INTRODUCTION

As a precurosr to our work, we need to start by discussing Whispering gallery mode (WGM) resonators, and cavity ringdown spectroscopy (CRDS). WGM resonators are known for their ease of fabrication, ultrahigh Q-factor, and stability. they have many applications[1] and could be employed as filters,[2–4] lasers ,,[5–7] and sensors.[8–14] WGM waves are confined to the outer circumference of a microcavity via total internal reflection; their evanescent tail is continuously scanning the cavity surface; this makes WGM resonators very useful for sensing applications. In a sensing event, the resonant wavelength or frequency of the cavity shifts according to the material under test. However, a major drawback, is that the interrogation of the WGM requires a tunable laser. The use of tunable lasers is problematic as they tend to be costly, bulky, and require frequency tracking.

Cavity Ringdown Spectroscopy (CRDS) is a well-researched technique that was created for the purpose of measuring mirror reflectivities and the optical properties of atoms,[15] and has been used to measure the absorption of gases in the atmosphere.[16–19] CRDS works by coupling a laser into a cavity and then turning the laser off; a fraction of the light is absorbed by the cavity, while the remainder leaks out of the cavity over a period of time known as the ringdown time; this ringdown time is directly related to the absorption of the test object. The CRDS output requires an exponential fitting algorithm which significantly increases the acquisition time. We can avoid this issue through using phase-shift CRDS (PS-CRDS). In PS-CRDS, a sinusoidal, amplitude-modulated, continuous-wave light source is injected to the cavity, thus producing an output with a phase-shift with respect

Further author information: (Send correspondence to Rania Gamal)
Rania Gamal: E-mail: rania.mohamed@mail.mcgill.ca

to the input; this shift is related to the ringdown time, by $tan\phi = \omega_m$, where $\phi$ is the phase shift and $\omega_m$ is the modulation frequency

PS-CRDS systems that employ a coherent source have a variety of applications and are well-researched.[20–22] A notable example of tunable laser-based PS-CRDS systems was demonstrated by Cheema *et al.*[23] where a microtoroid cavity was used to sense antibody-antigen binding in a liquid environment. In that work, light was coupled into a microtoroid via a tapered fiber. The Q-factor and resonant wavelength were measured simultaneously in real-time.[24] To demonstrate the validity of the model, we will present an example of our model based on Cheema's work.

In this paper, we aim to mathematically analyse the coherence properties of broadband PS-CRDS systems. By using a broadband source instead of tunable laser, the cost and complexity of the system can be significantly reduced.

The challenge presented in this work lies in determining the amount of phase-shift that can be produced by using an incoherent source. We will present a mathematical model that represents a partially coherent PS-CRDS system through employing Gabor's analytic signal representation.[25] In the first section, the microcavity system parameters are analyzed. The following section provides models for the CRDS and PS-CRDS interrogation mechanisms; in that section, the complex gain coefficient of the system is derived. The fourth and final section, presents an example of a PS-CRDS microcavity system to which the model developed in the former two sections is applied.

## 2. OVERVIEW OF THE MICROCAVITY SYSTEM

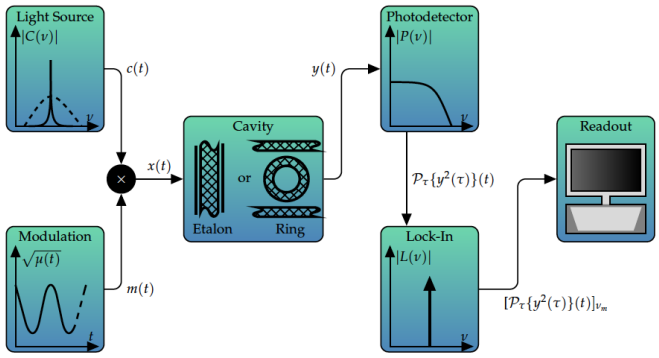


Figure 1. Phase-shift cavity ringdown spectroscopy system diagram.

The PS-CRDS system under investigation is shown in Figure 1; it comprises of a light source, an intensity modulator, a photodetector, a lock-in amplifier and an electronic read-out system. The light source is modulated by the carrier signal, which is an intensity-modulated sinusoidal signal. Afterwards, it is coupled into the cavity. The output signal intensity from the cavity is measured by the photodetector and then sent to a lock-in amplifier in order to remove all the spectral components that do not correspond to the frequencies of the input signal. Finally, post-processing of the output of the lock-in amplifier is performed by an electronic readout system. The goal of this work is to establish a relationship between the gain and phase of the output signal to the transmission properties of the cavity.

The input signal, $x(t)$, is the product of the carrier signal, $c(t)$, and the square root of the intensity modulation signal, or the amplitude modulation signal which is denoted by $m(t)$. For a CRDS system, $m(t)$ can be simply modelled as a unit step function. When $\mu(t)$ is continuous, as is the case in PS-CRDS, $m(t)$ is as follows:

$$m(t) = \sqrt{1 - h\sin^2(\pi\nu_m t + \frac{\phi_m}{2})}, \tag{1}$$

where $h = [0, 1]$ is the modulation depth, $\nu_m$ is the modulation frequency, and $\phi_m$ is an arbitrary phase factor.

We assume that the carrier signal, $c(t)$, has a Lorentzian energy spectral density. This assumption is reasonable since the majority of coherent optical sources, such as lasers, possess spectral densities that are very close to the Lorentzian distribution. The energy spectral density of the carrier is given by:

$$|C(\nu)|^2 = \frac{R_c(0)}{\pi\Delta\nu}\left[\frac{(\nu/2)^2}{(\nu-\nu_c)^2+(\Delta\nu/2)^2}+\frac{(\nu/2)^2}{(\nu+\nu_c)^2+(\Delta\nu/2)^2}\right], \tag{2}$$

where $R_c$ describes the autocorrelation of the carrier signal at zero delay, which describes the energy of the carrier signal, $\nu_c$ is the central frequency of the carrier signal, and $\Delta\nu$ is the full width at half maximum (FWHM) or the bandwidth of the carrier. To calculate the output power of the system, it is necessary to calculate the autocorrelation function of the analytic signal representation of the carrier signal, $\hat{c}(t)$, as it will later appear in the output of the photodetector. First, the autocorrelation of $c(t)$ is computed through computing the inverse Fourier transform of $|C(\nu)|^2$. Next, the autocorrelation of the analytic carrier signal is evaluated using the relation, $R_{\hat{z}}(\tau) = 2[R_z(\tau) + j\mathcal{H}_{t-\tau}\{R_z(t-\tau)\}(\tau)]$, where the symbol $\mathcal{H}\{x\}$ denotes the Hilbert transform of $x$, and $\tau$ represents a time delay. Finally, using Bedrosian's theorem,[26] the autocorrelation of $\hat{c}(t)$ can be described as:

$$R_{\hat{c}}(\tau) = 2R_c(0)e^{-\pi\Delta\nu|\tau|}e^{j2\pi\nu_c\tau} \tag{3}$$

This is the general autocorrelation function of $\hat{c}(t)$, and can be used to describe the behavior of a partially coherent $\hat{c}(t)$. The autocorrelation of a coherent $\hat{c}(t)$, and an incoherent $\hat{c}(t)$ can be calculated by taking the limit of $R_{\hat{c}}(\tau)$ as $\Delta\nu$ goes to zero, and infinity, respectively.

Now the next step is to study the output signal of the photodetector. We assume that the signal input to the photodetector has the intensity, $z^2(t)$. The photodetector's output, $P_\tau$, can, hence, be described as the convolution of the signal intensity with the impulse response, $p(t)$. The spectrum of the impulse response, $P(\nu)$, must have a finite bandwidth since photodetectors cannot respond instantaneously to their input. The response of LPFs in the time domain can be calculated as a moving average; thus, $p(t)$ can be approximated as $p(t) \approx 1$ if $t \in [0, T_p]$ or 0 othwerise, where $T_p$ is the response time of the photodetector. Therefore, $P_\tau\{z^2(\tau)\}(t) \approx \int_{t-T_p}^{t} d\tau z^2(\tau)$. Technically, $p(t)$ is a rect function, so the spectrum of $p(t)$ is a sinc function, but for our purposes, it will be assumed that $P(\nu)$ is zero at frequencies above $\nu_p \sim T_p^{-1}$ by explicitly approximating the spectrum as having a finite bandwidth, where $P(\nu) \approx P(\nu)$ if $\nu \in [-\nu_p, \nu_p]$, or 0 otherwise.

In order to relate $z^2(t)$ to $\hat{z}(t)$, the spectrum of $|\hat{z}(t)|^2$ is examined. By taking the Fourier transform of $|\hat{z}(t)|^2$, we find that $\mathcal{F}_t\{|\hat{z}(t)|^2\}(\nu) = 2\mathcal{F}_t\{z^2(t)\}(\nu) - 2\Psi_z(\nu)$, where $\Psi_z(\nu)$ is an error term. Hence, by taking the inverse Fourier transform, we get:

$$|\hat{z}(t)|^2 = 2z^2(t) - 2\psi_z(t) \tag{4}$$

where $\psi_z(t) = \mathcal{F}_\nu^{-1}\{\Psi_z(\nu)\}(t)$. Details concerning $\Psi_z(\nu)$ are rather complicated, so for the sake of brevity, we will only concern ourself with this conclusion: the approximate error term is zero for sufficiently small frequencies. If the reasonable assumption that $\lambda_c \leq 3000nm \rightarrow \nu_c \approx 10^{14}Hz$ is made, it can be claimed that $\tilde{\Psi}_z(\nu) = 0$ for $|\nu| \leq 10^{14}Hz$. The cut off frequency of a photodetector is at the most in the tens of gigahertz, so it can be also be claimed that $\tilde{P}(\nu) = 0$ for $|\nu| \geq 10^{10}Hz$. Therefore, the power contribution of the error term, $\mathcal{P}_\tau\{\psi_z(\tau)\}(t)$, is zero. Thus, the error term can be neglected, and the photodetector's response can be calculated as:

$$\mathcal{P}_\tau\{z^2(\tau)\}(t) \approx \frac{1}{2}\mathcal{P}_\tau\{|\hat{z}(\tau)|^2\}(t) \tag{5}$$

We will see that the photodetector's response to the argument $\hat{z}(t-\alpha)\hat{\bar{z}}(t-\beta)$ will appear in the upcoming derivations, where $\alpha$ and $\beta$ denote time delays introduced to the optical fields as they circulate within a cavity. Hence, the output power can be written as:

$$\begin{aligned}
&\mathcal{P}_\tau\{\hat{z}(\tau-\alpha)\hat{\bar{z}}(\tau-\beta)\}(t)\\
&\quad\approx \int_{\mathbb{R}} d\tau\, m(\tau-\alpha)m(\tau-\beta)\hat{c}(\tau-\alpha)\hat{\bar{c}}(\tau-\beta)p(t-\tau)\\
&\quad\approx m(t-\alpha)m(t-\beta)\int_{t-T_p}^{t} d\tau\, \hat{c}(\tau-\alpha)\hat{\bar{c}}(\tau-\beta)
\end{aligned} \tag{6}$$

The impulse response serves to set the limits of the integration. Additionally, the modulation signal varies slowly in comparison to the photodetector's response time, so it can be taken out of the integration. Also, note that $\hat{c}(t)$ is very quickly varying in comparison to the photodetector's response time, therefore, the integral in the previous equations is approximately independent of $t$ and $T_p$; therefore, the integration over $T_p$ is approximately proportional to an integration over the real line with a constant of proportionality $\mathcal{P}_{\hat{c}}$ independent of $t$, $\alpha$,and $\beta$. Consequently, the integration can be approximated as $\mathcal{P}_{\hat{c}}\int_{\mathbb{R}} d\sigma \hat{c}(\sigma)\hat{\bar{c}}(\sigma-[\beta-\alpha])$, where $\sigma := \tau-\alpha$. Observe how the autocorrelation function appeared in the detector output as has been mentioned beforehand. Finally, the output power of the detector is given by:

$$\mathcal{P}_\tau\{\hat{z}(\tau-\alpha)\hat{\bar{z}}(\tau-\beta)\}(t) \approx m(t-\alpha)m(t-\beta)\mathcal{P}_{\hat{c}}R_{\hat{c}} \tag{7}$$

We now consider a cavity in the form of a four-port ring resonator with input $\hat{x}(t)$ and output $\hat{y}(t)$. The ring resonator is made of a material with refractive index $n$ and transmission coefficient $t_n$. The half circumference of the ring is denoted by $d$. The length travelled by the light wave from one coupling region to the next, or the optical path length is given by $\ell := nd$. The time it takes to travel that distance is given by $\Delta t := \ell/c_0$ . The transmission and coupling coefficients of the evanescent wave coupling region are denoted by $\tau_i$ and $\kappa_i$. It is assumed that the ring-resonator dissipates the fields going through it. Generally, the output of the ring resonator is the summation of each input field multiplied by the coupling and transmission coefficients. By calculating the first few iterations of the light wave within the resonator, it is found that:

$$\hat{y}(t) = \kappa_1\kappa_2 t_n \sum_{k\in\mathbb{N}} [\tau_1\tau_2 t_n^2]^k \hat{x}(t-[2k+1]\Delta t) \tag{8}$$

The effective transmittance is defined as $\mathcal{T} := \kappa_1\kappa_2 t_n$; the effective reflectance, on the other hand, is defined as $\mathcal{R} := \tau_1\tau_2 t_n^2$. Additionally, odd multiples of the time delay can be denoted by $\Delta t_k := [2k+1]\Delta t$ for $k \in \mathbb{N}$. We need to rewrite the output of the ring resonator as an intensity, in order to computer the photodetector's response:

$$|\hat{y}(t)|^2 = |\mathcal{T}|^2 \sum_{k,\in\mathbb{N}} \sum_{l\in\mathbb{N}} \mathcal{R}^k \mathcal{R}^{-l} \hat{x}(t-\Delta t_k)\hat{\bar{x}}(t-\Delta t_l) \tag{9}$$

In order to evaluate the output power of the photodetector, the following steps are taken: first, equation 6 is used to compute $\mathcal{P}_\tau\{y^2(\tau)\}(t)$. Next, the carrier autocorrelation function, $R_{\hat{c}}$, appears through the use of equation 7. Then, $R_{\hat{c}}$ is reformulated using equation 3. Finally, the output power of the photodetector is described as follows:

$$\mathcal{P}_\tau\{y^2(\tau)\}(t) \approx |T_c|^2 \sum_{k\in\mathbb{N}} \sum_{l\in\mathbb{N}} \mathcal{R}_c^k \mathcal{R}_c^{-1} e^{-\Delta|l-k|} m(t-\Delta t_k)m(t-\Delta t_l) \tag{10}$$

where the terms $\mathcal{T}_c, \mathcal{R}_c$, and $\Delta$ are used to approximate the above expression; $\mathcal{T}_c := \mathcal{T}\sqrt{R_c(0)\mathcal{P}_{\hat{c}}}, \mathcal{R}_c := \mathcal{R}e^{-j4\pi\nu_c\Delta t}$, and $\Delta := 2\pi\Delta\nu\Delta t$. The power of the input signal can be obtained in a similar fashion and will yield:

$$\mathcal{P}_\tau\{x^2(\tau)\} \approx R_c(0)\mathcal{P}_{\hat{c}} m^2(t) \tag{11}$$

## 3. ANALYTICAL MODEL OF CAVITY-BASED SYSTEMS

Now that we have described all the signals in our system, we now need to derive the input and output power for CRDS and PS-CRDS. These calculations are necessary for understanding the coherence effects on the system.

### 3.1 Power and Gain Calculations

In a CRDS system, the light source is turned on and then off, therefore, the carrier will be modelled as a unit step function. From equation (11), it can be concluded that the input modulated signal for CRDS is derived as follows:

$$\mathcal{P}_\tau\{x^2(\tau)\}(t) \approx R_c(0)\theta^2(-t) = [R_c(0)\mathcal{P}_{\hat{c}}]\theta(-t) \tag{12}$$

where $\theta$ denotes the unit step function.

In a similar fashion, the output can be derived by inserting the unit step function into equation (10). After some calculations, we conclude that:

$$\mathcal{P}_\tau\{y^2(\tau)\}(t) \approx R_c(0)\mathcal{P}_{\hat{c}}\mathcal{G}|\mathcal{R}|^{2N(t)}, \tag{13}$$

where $N(t) := \left\lceil \frac{(t-\Delta t)}{2\Delta t} \right\rceil \theta(t-\Delta t)$, and $\mathcal{G}$ is the gain, and is given by:

$$\mathcal{G} = \frac{1-|\mathcal{R}|^2 e^{-2\Delta}}{1-|\mathcal{R}|^2} \left\{ \frac{|\mathcal{T}|^2}{2|(1-\mathcal{R}|e^{-\Delta}\cos(2\phi_c - \angle\mathcal{R}) + |\mathcal{R}|^2 e^{-2\Delta})} \right\} \tag{14}$$

Expressing equation (13) in terms of an exponential yields the output model:

$$\mathcal{P}_\tau\{y^2(\tau)\}(t) \approx [R_c(0)\mathcal{P}_{\hat{c}}]\mathcal{G}e^{-2\ln(\frac{1}{\mathcal{R}})N(t)} \tag{15}$$

Hence, the ringdown time of the cavity can be written as,

$$\tau_0 := \frac{\Delta t}{\ln(1/|\mathcal{R})} \tag{16}$$

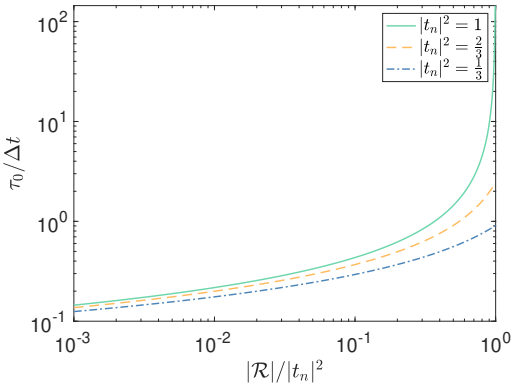


Figure 2. Relationship between $\tau_0/\Delta t$ and $|\mathcal{R}|/|t_n|^2$ for identical and lossless interfaces for CRDS

The dependence of the ringdown time on the value $|\mathcal{R}|/|t_n|^2$ is shown in Figure 2 for three values of $—t_n|^2$. It can be seen that as the effective reflectance increases, the cavity confines light for longer periods of time, hence, lengthening the ringdown time.

It is challenging to express the measured output in closed-form due to the square root in equation (1). Hence, we will resort to using an approximation of the modulation signal for the PS-CRDS system:

$$\tilde{m}(t) = \left(\frac{1+\sqrt{1-h}}{2}\right) + \left(\frac{1-\sqrt{1-h}}{2}\right) cos(2\pi\nu_m t + \phi_m) \tag{17}$$

Next, equation (17) in plugged into equation (10) to produce the output of the lock-in amplifier,

$$[\mathcal{P}_\tau\{y^2(\tau)\}(t)]_{\nu_m} \approx \left[\frac{R_c\mathcal{P}_{\hat{c}}h}{2}\right]|\Gamma|\cos(2\pi\nu_m t + \phi_m + \angle\Gamma) \tag{18}$$

where we introduce the complex gain coefficient, $\Gamma$, as

$$\begin{aligned}\Gamma :=& \frac{|\mathcal{T}|^2 e^{-j\varphi_m}}{1-|\mathcal{R}|^2\exp^{-j2\varphi_m}} \\ & \left\{\frac{1}{2}\left[\frac{1}{1-|\mathcal{R}|e^{-\Delta}e^{-j(2\varphi_m+2\varphi_c-\angle\mathcal{R})}}\right.\right. \\ & \left. + \frac{1}{1-|\mathcal{R}|e^{-\Delta}e^{-j(2\varphi_m-2\varphi_c+\angle\mathcal{R})}}\right] \\ & \left. + \Re\left[\frac{1}{1-|\mathcal{R}|e^{-\Delta}\exp^{-j(2\varphi_c-\angle\mathcal{R})}}\right] - 1\right\}\end{aligned} \tag{19}$$

where $\varphi_m := 2\pi\nu_m\Delta t$ and $\varphi_c := 2\pi\nu_c\Delta t$.

Similarly, the input power can be obtained by inserting equation (17) into equation (11), which yields,

$$[\mathcal{P}_\tau\{x^2(\tau)\}(t)]_{\nu_m} \approx \left[\frac{R_c(0)\mathcal{P}_{\hat{c}}h}{2}\right]\cos(2\pi\nu_m t + \phi_m) \tag{20}$$

### 3.2 Temporal Coherence Studies

Now, it is possible to study the model's prediction for an incoherent carrier. To achieve this, the limit of the frequency as it tends to infinity was taken for the complex gain coefficient. This process yields:

$$\Gamma|_{\Delta\nu\to\infty} := \lim_{\Delta\nu\to\infty}\Gamma = \frac{|\mathcal{T}|^2 e^{-j\varphi_m}}{1-|\mathcal{R}|^2 e^{-j2\varphi_m}} \tag{21}$$

Figure 3 plots the PS-CRDS phase shift versus the modulation frequency for three values of $|t_n|$. Here, the interfaces of the cavity are assumed to be identical and lossless, and $|\mathcal{R}|/|t_n|^2$ is taken as 0.99; these assumptions will be held throughout this section. The downward trend occurs because of the time delay experienced by the signal when travelling a distance equal to the optical path length. On the other hand, the cavity dynamics introduce oscillatory deviations around $\angle\Gamma = -\pi(\nu_m/FSR)$. Note that for a unity $|t_n|$, the phase shift is discretized into odd multiples of $\pi/2$ and decreases by a factor of $\pi$ when the modulation frequency is increased by a single FSR. Moreover, as $|t_n|$ is reduced, the phase shift shows a more linear relationship with the modulation frequency.

Figure 4 depicts the scaling of the measured output with respect to the input versus the modulation frequency for three values of $|t_n|$. As can be expected, a smaller transmission coefficient leads to a smaller output. The maxima occur when $\angle\Gamma = -\pi(\nu_m/FSR)$; this happens because the intensity of the signal entering the cavity can be in or out of phase with the intensity of the reflections within the cavity. When the modulation frequency

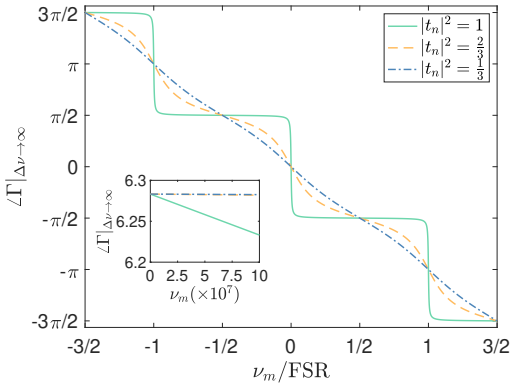


Figure 3. Phase-shift of incoherent carrier vs. modulation frequency per FSR for different transmission coefficients.

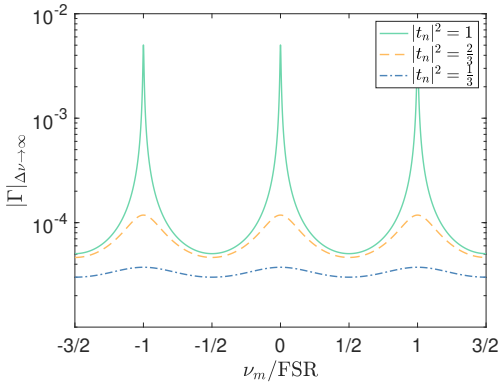


Figure 4. Output scaling of incoherent carrier vs. modulation frequency per FSR for different transmission coefficients.

is an integer multiple of the FSR, the intensity of the signal entering the cavity is perfectly in phase with the reflections within the cavity. As for the coherent carrier, the complex gain coefficient is defined as:

$$\begin{aligned}\Gamma|_{\Delta\nu=0} :=& \frac{|\mathcal{T}^2|e^{-j\varphi_m}}{1-|\mathcal{R}|^2\exp^{-j2\varphi_m}} \\ & \left\{\frac{1}{2}\left[\frac{1}{1-|\mathcal{R}|e^{-j(2\varphi_m+2\varphi_c-\angle\mathcal{R})}}\right.\right. \\ & \left.\left.+\frac{1}{1-|\mathcal{R}|e^{-j(2\varphi_m-2\varphi_c+\angle\mathcal{R})}}\right]\right. \\ & \left.+\Re\left[\frac{1}{1-|\mathcal{R}|\exp^{-j(2\varphi_c-\angle\mathcal{R})}}\right]-1\right\}\end{aligned} \tag{22}$$

We now introduce the fractional part function, where $frac(t) := t - k$, where $k \in Z$ such that $0 \leq t - k \leq 1$.

Figure 5 shows the phase shift versus the modulation frequency for three values of the carrier frequency. The transmission coefficient was set to unity in order to focus on the effects of $\nu_m$ and $\nu_c$. Similar to the case with the incoherent carrier, the phase shift is clamped to integer multiples of $\pi/2$ based on the modulation frequency. Similarly, the curves follow a downward trend.

Figure 6 exhibits $\Gamma|_{\Delta\nu=0}$ with respect to the modulation frequency for three values of the carrier frequency. Here, the values of $\nu_m$ where the sharp cusps occur correspond to the locations where $\angle\Gamma|_{\Delta\nu=0}$ abruptly changes.

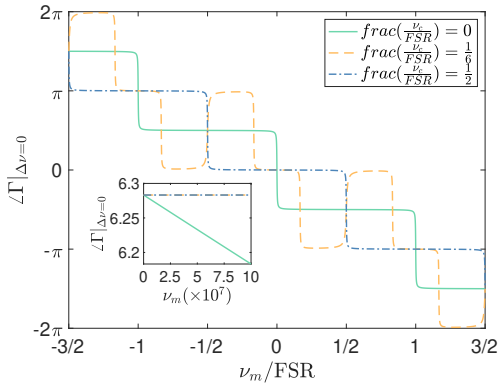


Figure 5. Phase-shift of coherent carrier vs. modulation frequency per FSR for carrier frequencies.

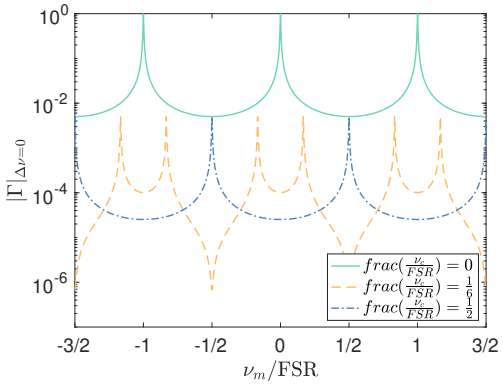


Figure 6. Output scaling of coherent carrier vs. modulation frequency per FSR for different carrier frequencies.

There is a strong dependence of $\Gamma|_{\Delta\nu=0}$ on the relative detuning of the carrier with respect to the cavity's spectrum; the spectrum of the cavity, $\mathcal{G}|_{\Delta\nu=0}$ plays an important role in understanding this behavior. When $\nu_c$ is located at a peak of $\mathcal{G}|_{\Delta\nu=0}$, there will be a maximum in the output whenever $\nu_m$ is an integer multiple of the FSR ($frac(\nu_c/FSR) = 0$). On the other hand, when $\nu_c$ is located at the minimum of $\mathcal{G}|_{\Delta\nu=0}$, there is a maximum in the output whenever $\nu_m$ is an odd integer multiple of $FSR/2$ ($frac(\nu_c/FSR) = 1/2$). For the third and final case, there are two peaks since each side band of $X(\nu)$ corresponds to a peak in $\mathcal{G}|_{\Delta\nu=0}$ at a different $\nu_m$. Note that the spectrum, $X(\nu)$, consists of two deltas positioned at $(\nu_c - \nu_m)$ and $(\nu_c + \nu_m)$.

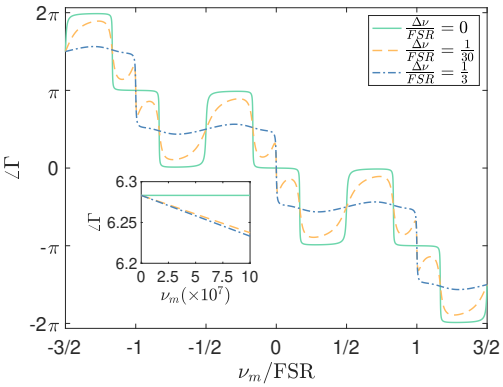


Figure 7. Phase-shift of partially coherent carrier vs. modulation frequency per FSR for different carrier frequencies.

Lastly, for a partially coherent carrier, equation (19) is used. It is also be assumed that ($frac(\nu_c/FSR) =$

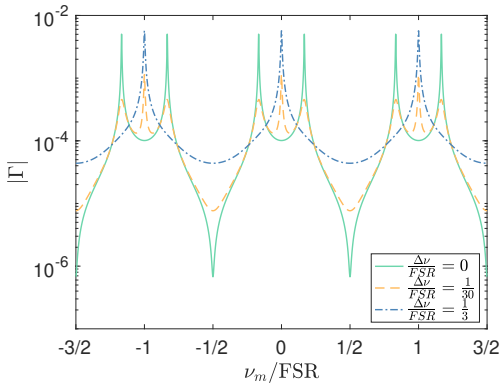


Figure 8. Output scaling of partially coherent carrier vs. modulation frequency per FSR for different carrier frequencies.

1/6). Figures 7 and 8 illustrate the phase shift and the output scaling versus the modulation frequency, respectively. It is clear that as the carrier linewidth is increased, the behavior of the curves start to resemble the incoherent case. As the bandwidth increases, a larger portion of the cavity spectrum contributes to the measured output, which blurs out the exact location of the carrier frequency.

## 4. VERIFICATION OF PROPOSED MODEL

To verify the information presented so far, the principles that were previously stipulated were applied to characterize the system presented in.[23] This system comprises a silica microtoroid that employs a tapered fiber for coupling. The system parameters and assumptions made, are listed in Table 1. The optical source used in this system is the Velocity TLB-6704 tunable laser by New Focus;[27] for this source, the carrier signal is centered at 472 THz with a bandwidth of approximately 200 kHz. By virtue of its very narrow linewidth, this source can be approximated as a coherent source. Furthermore, to study coherence effects, we model the partially coherent source after a laser diode (WSLP-635-002m-Pm-PD[28]); the peak wavelength of this laser diode is centered between 630 nm and 640 nm, so for simplicity, we will assume it is located at the resonant wavelength of the cavity; the bandwidth is about 1.48 THz.

Table 1. Microtoroid Parameters

| Parameter | Value | Description |
|---|---|---|
| D | $105\mu m$ | Diameter |
| $\lambda_{peak}$ | $636nm$ | Resonant Wavelength |
| $\delta\lambda$ | $210fm$ | Peak Width |
| $n$ | 1.45693 | Refractive Index |
| $t_n$ | 1 | Transmission Coefficient |
| FSR | $624GHz$ | Free Spectral Range |
| $\tau_1 = \tau_2$ | in $\mathbb{R}$ | Coupler Transmission Coefficient |

The gain (equation (14)) of the system is explored in Figure 9, where it is seen that there is an inverse relation between the gain and $|t_n|$. Additionally, the gain for the laser diode is roughly three orders of magnitude less than the gain for the tunable laser; this severe attenuation is due to the significantly smaller amount of energy in the laser diode's spectrum that corresponds with the cavity's resonance.

The response of the gain to a variation in the refractive index was also studied. It was found that for a sufficiently large refractive index change ($\Delta n \approx 2 \times 10^{-7}$), the gain factor for the tunable laser starts to decrease; this behavior occurs because the increase in $n$ causes a decrease in the cavity's FSR; this causes the resonant

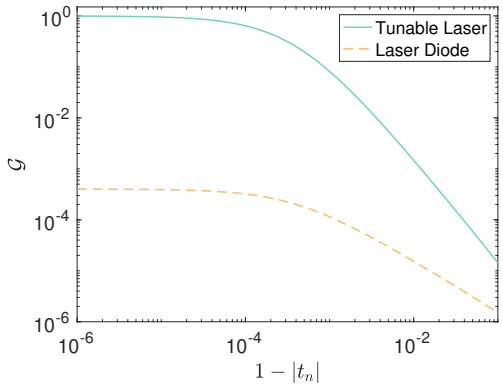


Figure 9. Relationship between gain and coupling coefficient for tunable laser and laser diode.

frequency to detune from the tunable laser's central frequency. Nevertheless, the laser diode appears to be completely insensitive to variations in the refractive index; in this case, even if the cavity's resonant peaks shift due to the increase in $\Delta n$, approximately the same number of peaks fall within the carrier bandwidth.

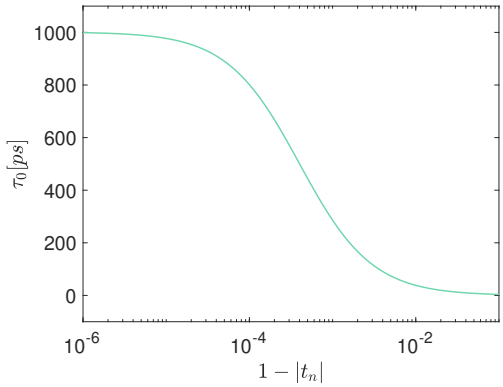


Figure 10. Relationship between ringdown time and transmission coefficient.

Next, we will focus on the behavior of the ringdown time. Figure 10 shows a plot of the ringdown time as a function of the microtoroid transmission coefficient. Since the ringdown time is independent of the carrier bandwidth, the behavior the tunable laser and the laser diode will be identical. As expected, the ringdown time decreases as the transmission coefficient decreases. The response of the ringdown time to changes in the cavity's refractive index was also explored. Generally, the ringdown time does not vary for small changes in the refractive index, but for changes larger than $\Delta n \approx 10^{-5}$, the ringdown time increases exponentially.

Next, the complex gain coefficient for the system is evaluated. For this purpose, the frequency modulation is set as 13 MHz, as was the case in.[?] Figure 11 depicts the change in $\angle\Gamma$ as the transmission coefficient is varied. The phase shift of the tunable laser and the laser diode turn out to be sensitive to changes in $|t_n|$; more so, the phase shift of the tunable laser is roughly twice that of the laser diode. This phenomenon can be attributed to the fact that the very small linewidth of the tunable laser is strongly influenced by the cavity's resonance, whereas, the bandwidth of the laser diode interacts with several peaks in the cavity's response which leads to cancellation from the contributions of different parts of the cavity's spectrum.

In Figure 12, the output scaling as a function of $|t_n|$ is shown. Less energy exits the cavity due to absorption and scattering effects, as the transmission coefficient is reduced; this results in a decrease in $|\Gamma|$ for both sources. As would be expected, the output scaling for the laser diode is considerably smaller—roughly three orders of magnitude—than that of the tunable laser.

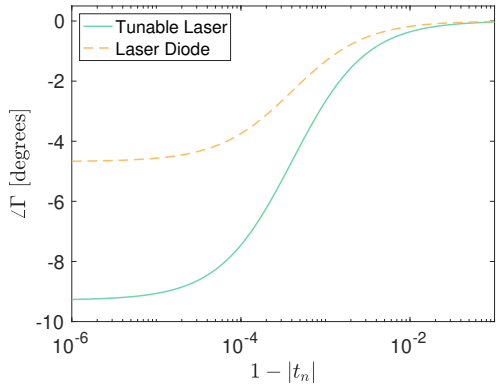


Figure 11. Phase-shift vs. transmission coefficient for tunable laser and laser diode.

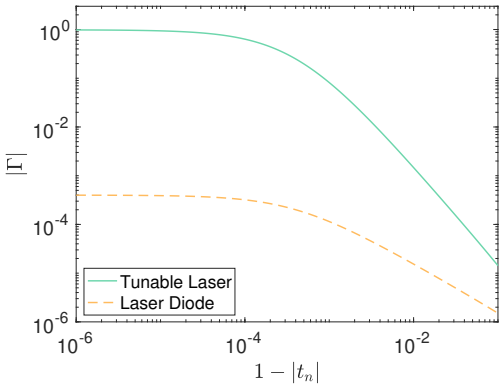


Figure 12. Output scaling vs. transmission coefficient for tunable laser and laser diode.

Lastly, the complex gain coefficient was evaluated against refractive index variation ($\Delta n = [10^{-9}, 10^{-4}]$). It is found that the phase shift and output scaling of the laser diode are completely insensitive to variations in the refractive index due to the reason discussed in the ringdown time's response to $\Delta n$. On the other hand, $|\Gamma|$ and $\angle\Gamma$ appear to be measurable for the tunable laser in the range $10^{-7} \leq \Delta n \leq 10^{-6}$ by virtue of the peaks in cavity spectrum detuning from the narrow linewidth of the laser signal.

## 5. CONCLUSION

We studied the effects of temporal coherence on CRDS and PS-CRDS in order to anticipate the performance of a broadband PS-CRDS sensor system. We found that the bandwidth of the laser has a significant effect on the performance and measurability of certain parameters. A significant discovery is that systems with less coherent sources are insensitive to refractive index variations, however, they are sensitive to absorption. Therefore, for a broadband biosensing PS-CRDS system, the biosensing event must induce some absorption in order for the system to work. For CRDS, larger source bandwidths generally result in a smaller output power. Alternately, the effect of the source bandwidth of a PS-CRDS system on the output power depends on the values of carrier and modulation frequencies. These reported dynamics should be taken into consideration when designing a cavity-based spectroscopy system with a partially coherent source.

## REFERENCES

[1] [*Review of Applications of Whispering-Gallery Mode Resonators in Photonics and Nonlinear Optics*] (2005).

[2] Little, B. E., Chu, S. T., Pan, W., Ripin, D., Kaneko, T., Kokubun, Y., and Ippen, E., "Vertically coupled glass microring resonator channel dropping filters," *IEEE Photonics Technology Letters* **11**, 215–217 (Feb. 1999).

[3] Savchenkov, A. A., Ilchenko, V. S., Matsko, A. B., and Maleki, L., "High-order tunable filters based on a chain of coupled crystalline whispering gallery-mode resonators," *IEEE Photonics Technology Letters* **17**, 136–138 (Jan. 2005).

[4] Savchenkov, A., Ilchenko, V., Matsko, A. B., and Maleki, L., "Tunable optical filters having electro-optic whispering-gallery-mode resonators," (Aug. 2006).

[5] McCall, S. L., Levi, A. F. J., Slusher, R. E., Pearton, S. J., and Logan, R. A., "Whispering-gallery mode microdisk lasers," *Applied Physics Letters* **60**, 289–291 (Jan. 1992).

[6] Harayama, T., Davis, P., and Ikeda, K. S., "Whispering Gallery Mode Lasers," *Progress of Theoretical Physics Supplement* **139**, 363–374 (May 2000).

[7] Sandoghdar, V., Treussart, F., Hare, J., Lefèvre-Seguin, V., Raimond, J. M., and Haroche, S., "Very low threshold whispering-gallery-mode microsphere laser," *Physical Review A* **54**, R1777–R1780 (Sept. 1996).

[8] "Towards more accurate microcavity sensors: maximum likelihood estimation applied to a combination of quality factor and wavelength shifts," **21**.

[9] Vollmer, F. and Arnold, S., "Whispering-gallery-mode biosensing: label-free detection down to single molecules," *Nature Methods* **5**, 591–596 (July 2008).

[10] Vollmer, F., Arnold, S., and Keng, D., "Single virus detection from the reactive shift of a whispering-gallery mode," *Proceedings of the National Academy of Sciences* **105**, 20701–20704 (Dec. 2008).

[11] Maleki, L. and Ilchenko, V., "Optical sensing based on whispering-gallery-mode microcavity," (Dec. 2002).

[12] Foreman, M. R., Swaim, J. D., and Vollmer, F., "Whispering gallery mode sensors," *Advances in Optics and Photonics* **7**, 168–240 (June 2015).

[13] Lin, N., Jiang, L., Wang, S., Xiao, H., Lu, Y., and Tsai, H., "Thermostable refractive index sensors based on whispering gallery modes in a microsphere coated with poly(methyl methacrylate)," *Applied Optics* **50**, 992 (Mar. 2011).

[14] Lutti, J., Langbein, W., and Borri, P., "A monolithic optical sensor based on whispering-gallery modes in polystyrene microspheres," *Applied Physics Letters* **93**, 151103 (Oct. 2008).

[15] Miller, G. P. and Winstead, C. B., "Cavity Ringdown Laser Absorption Spectroscopy," in [*Encyclopedia of Analytical Chemistry*], American Cancer Society (2006).

[16] Atkinson, D. B., "Solving chemical problems of environmental importance using cavity ring-down spectroscopy," *Analyst* **128**, 117–125 (Feb. 2003).

[17] Brown, S. S., "Absorption spectroscopy in high-finesse cavities for atmospheric studies," *Chemical Reviews* **103**, 5219–5238 (Dec. 2003).

[18] Crosson, E. R., "A cavity ring-down analyzer for measuring atmospheric levels of methane, carbon dioxide, and water vapor," *Applied Physics B* **92**, 403–408 (Sept. 2008).

[19] Bitter, M., Ball, S. M., Povey, I. M., and Jones, R. L., "A broadband cavity ringdown spectrometer for in-situ measurements of atmospheric trace gases," *Atmos. Chem. Phys.* **5**(9).

[20] Cheema, M. I., Khan, U. A., Armani, A. M., and Kirk, A. G., "Application of phase shift ring down spectroscopy to microcavities for biosensing," in [*Nanoscale Imaging, Sensing, and Actuation for Biomedical Applications X*], **8594**, 859401, International Society for Optics and Photonics (Feb. 2013).

[21] Dhiman, C., Khan, M. S., and Reddy, M. N., "Phase-shift Cavity Ring-down Technique for Detection of NO2 in PPM Concentration," *Defence Science Journal; New Delhi* **64**, 426–430 (Sept. 2014).

[22] Reid, G. D., Robertson, M. D., and Tong, A. Z., "Derivation of New Equations for Phase-Shift Cavity Ring-Down Spectroscopy," *The Journal of Physical Chemistry A* **115**, 4902–4908 (May 2011).

[23] Cheema, M. I., Mehrabani, S., Hayat, A. A., Vanier, F., Peter, Y.-A., Armani, A. M., and Kirk, A. G., "Experimental demonstration of application of ring down measurement approach to microcavities for biosensing," in [*Frontiers in Biological Detection: From Nanosensors to Systems IV*], **8212**, 82120B, International Society for Optics and Photonics (Feb. 2012).

[24] Cheema, M. I., Mehrabani, S., Hayat, A. A., Peter, Y.-A., Armani, A. M., and Kirk, A. G., "Simultaneous measurement of quality factor and wavelength shift by phase shift microcavity ring down spectroscopy," *Optics Express* **20**, 9090–9098 (Apr. 2012).

[25] Gabor, D., "Theory of communication. Part 1: The analysis of information," *Journal of the Institution of Electrical Engineers - Part III: Radio and Communication Engineering* **93**, 429–441 (Nov. 1946).

[26] Bedrosian, E., "A Product Theorem for Hilbert Transforms," (1962).
[27] "Velocity 6700 Widely Tunable Lasers."
[28] "WSLP-635-002m-PM-PD."